NJC

The Doorstop Proton: Acid-controlled Photoisomerization in Pyridine-Based Azo Dyes

Journal:	*New Journal of Chemistry*
Manuscript ID	NJ-ART-04-2023-001769.R1
Article Type:	Paper
Date Submitted by the Author:	25-May-2023
Complete List of Authors:	Martin, Shea; Lehigh University, Department of Chemisry Knepp, Zachary; Lehigh University, Department of Chemistry Thongchai, Ing; Lehigh University, Department of Chemistry Croland, Kiera; Lehigh University, Department of Chemistry Sorto, Keyri; Lehigh University, Department of Chemistry Jaffer, Athina; Lehigh University, Department of Chemisry Fredin, Lisa; Lehigh University, Lisa Fredin; Young, Elizabeth; Lehigh University, Department of Chemistry

ARTICLE

The Doorstop Proton: Acid-controlled Photoisomerization in Pyridine-Based Azo Dyes

Received 00th January 20xx,
Accepted 00th January 20xx

DOI: 10.1039/x0xx00000x

Shea M. Martin, Zachary J. Knepp, Ing Angsara Thongchai, Kiera Englehart, Keyri Sorto, Athina Jaffer, Lisa A. Fredin,* Elizabeth R. Young*

The photochemical properties and straightforward synthesis of a wide range of azo dyes has led to their use in a wide range of applications. Despite their broad use, the fundamental structure-function relationships of many variants are unexplored. Here, azo dyes with a pyridine moiety are systematically investigated. The pyridine affords a range of electronic effects due to the position of the nitrogen heteroatom relative to the azo bond and serves as a second protonatable site in addition to the azo bond that provides a way to alter the isomerization yield of the dye through inductive effects and protonation in addition to the azo bond. Photometric titrations, visible-light photoisomerization, and density functional theory (DFT) calculations reveal and rationalize the unexpected loss of photoisomerization that occurs upon protonation of the pyridine N (the first protonation site on the pyridine-based azo dyes). The result is particularly surprising as this site is not adjacent to or on the azo bond and yet it completely shut downs bulk photoisomerization. The first protonation of the azo dyes onto the pyridine N results in a red shift of the spectra by 132 nm, 64 nm and 106 nm for Pyr2, Pyr3, and Pyr4, respectively. The second protonation onto the azo bond blueshifts the spectra by 102 nm, 19 nm, and 89 nm, respectively. pK_a values of the pyridine N are 14.9, 14.6 and 15.3, while the pK_a values of the azo bond N are 11.3, 11.4, and 13.8, for Pyr2, Pyr3, and Pyr4, respectively. DFT reveals that the loss of photoisomerization arises from both a reduction in the generated *cis*-isomer upon photoexcitation and an accelerated *cis* to *trans* reversion process on the ground state potential energy surface.

Introduction.

Azo dyes have been the target of a significant amount of research in recent years due to their ubiquitous use as textile pigments,[1] synthetic chemical precursors,[2] and cosmetics.[3] One focus of these studies has been to reduce the environmental impact of toxic azo dyes and their byproducts from industrial processes.[4–12] However, the fundamental understanding of the impact of substituents and heteroaryl groups on the physical and chemical properties of azo dyes is still underexplored.[13–15] Early spectroscopic experiments reported that many azo dyes undergo a *trans* → *cis* photoisomerization[1,13–17] upon excitation with blue or UV light, which can be exploited for photoswitching applications.[18–22] Subsequent studies present detailed investigation shedding light on the mechanism of photoisomerization in azo dyes.[23–30] It is generally accepted that when azobenzene is illuminated, the decay of the initial photoexcited state occurs through a torsional rotation of the ∠CNNC dihedral resulting in population of the higher energy *cis*-isomer.[16] Kovalenko and coworkers performed a thorough analysis of unsubstituted azobenzene using a combination of transient absorption, fluorescence, stimulated Raman spectroscopy and computational methods.[28] They assigned the observed ultrafast dynamics to an isomerization *via* a hula-twist

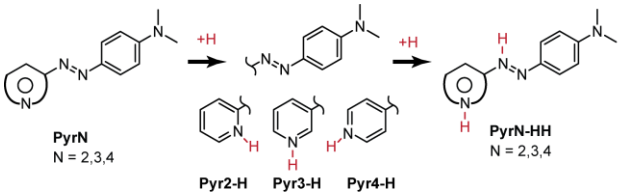

Figure 1. Chemical structures of dyes **Pyr2**, **Pyr3**, **Pyr4**, and corresponding singly protonated (**Pyr2-H**, **Pyr3-H**, **Pyr4-H**) and doubly protonated (**Pyr2-HH**, **Pyr3-HH**, **Pyr4-HH**) species.

[a] 6 E. Packer Ave., Bethlehem, PA 18015, USA.
† Footnotes relating to the title and/or authors should appear here.
Electronic Supplementary Information (ESI) available: titrations and fittings, NMR, pK_a values, and additional computational results including molecular orbitals, calculated energies, and potential energy curves. See DOI: 10.1039/x0xx00000x

mechanism which differs slightly from either of the better known rotational or inversional mechanisms.[28] Ground state *cis* reverts thermally to the *trans*-isomer through an inversion (CNN bond angle) on the ground state potential energy surface (S_0).[16] While this mechanism has been investigated for symmetric azobenzene,[31] the effects of substitutions and asymmetry around the azo bond need to be more fully explored.

The nitrogens of the azo bond provide natural protonation sites, the protonation of which would geometrically hinder the photochemical or thermal isomerization of the dye. Indeed, such protonation has been used to hinder or control molecular degrees of freedom in past work.[42] Hydrazone-based azo dyes offer a readily accessible protonation site with an oxygen near the azo bond that, through hydrogen-bonding interactions, locks in a specific isomer by blocking inversion or rotation of the azo bond. Multiple protonation sites have been exploited to access interesting photochemistry involving isomerization about the C-N axes adjacent to the azo bond via direct interaction with the azo bond itself. Aprahamian and coworkers initially demonstrated hydrazone-based azo dyes with both quinolinyl and pyridyl rings that were able to form multi-point hydrogen bonds involving the azo bond nitrogens upon protonation.[38,39] The hyrdazone rotational isomer (E/Z) was tunable through a change in protonation state[38] or coordination to a Zn^{2+} metal center.[39] In particular, Antonov and coworkers reported that the rotational isomer can be switched using UV photons and involved in long-range proton transfer.[40,41] Likewise, metal ions can be used to control the conformation or lock particular molecular structures in place as demonstrated by the work of Giorgiev and coworkers who reported that the binding of an N heteroatom to Zn^{2+} or azo bond protonation allows for the tuning of the isomerization and photoluminescent properties of their pyridine- and isoquinoline-based dyes.[42]

In addition, redox chemistry is controlled by protonation of the azo bond. For example, anthracene-based azo dyes undergo proton-coupled electron transfer (PCET) processes[32,33] in which the addition of as little as one equivalent of various organic acids substantially increased (smaller negative values) the electrochemical reduction potential of the dye in a concerted PCET event.[32] Using a potential-pK_a plot, the pK_a-dependent region (in acetonitrile) was identified between pK_a 8.6 – 20.35 in which the reduction potential of the anthracene-based azo dye increased as the acid strength increased with a slope of 75 mV per decade, indicative of a 1 H^+/1 e^- concerted PCET event.[32] Upon protonation with a strong enough acid (pK_a below ~8 in acetonitrile), the reduction potential was increased by ~1 volt compared to the unprotonated version. Based on this initial work, we thought that the addition of acid to protonate azo dyes could also be used to control the photophysical evolution of azo dyes.

Along these lines, the electrochemical and photophysical properties of other azo dyes have been shown to be impacted by the addition of acid.[13,16,17,22,32–37] Photoisomerization of protonated azobenzene and *para*-aminoazobenzene in the gas phase was observed by Bieske and coworkers using tandem ion mobility spectroscopy to obtain photoisomerization action (PISA) spectra [35]. They showed that the protonated dye could be observed in the *cis*-isomer, and computationally identified that protonation of both species occurred on an azo nitrogen.[35] Kortekaas and coworkers found that protonation of *para*-methoxyazobenzene resulted in a redshifted absorption spectrum.[34] The unprotonated dye isomerized to the *cis*-isomer under UV illumination. While small yields of protonated *cis* p-methoxyazobenzene was observed upon protonation with strong acids, protonation of the azo bond with weaker acids reduced the extent of observable photoisomerization. Interestingly, reversion of the protonated species was induced by UV illumination. Winnik and coworkers described the *cis*-to-*trans* reversion rate of an azopyridine-terminated amide-functionalized polymer that had the potential to undergo intramolecular hydrogen bonding between the amide nitrogen and the pyridine nitrogen. They revealed that the polymer reverted from the *cis*-isomer significantly faster at low pH ranges ($t_{1/2}$ = 2.3 ms at pH = 3.0) than in more alkaline conditions ($t_{1/2}$ >3600s at pH = 10).[37] These studies demonstrated that protonation of azo dyes affects their photophysical properties in ways that are only beginning to be understood.

Azobenzene and its derivatives have also been incorporated into polymers, either in the backbone or as a pendant group, to create photoresponsive materials that find applications as optical storage media and light-driven machinery.[43–50] Again, azopyridine is an attractive pendant group due to its hydrogen bonding ability. The hydrogen bonding network allows polymers containing this building block to form unique supramolecular architectures that expand polymer functionality. Cui and Zhao reported the synthesis of an azopyridine functionalized methacrylate polymer that showed suprastructural formation with a variety of carboxylic acids.[45] When deposited in thin films, the azo bonds in these polymers isomerized, which caused a decrease in optical transmission that slowly returned upon thermal reversion.[45] Yu and coworkers reported the self-assembly and photoresponsive behavior of a supramolecular organo-gel composed of an oleic acid / azopyridine-functionalized methacrylate copolymer.[43] UV irradiation transformed the gel into a colorless liquid. The gel reformed slowly when illumination was removed. The photoresponse was attributed to the isomerization and reversion of the azopyridine groups.[43] In polymers, azopyridine combines the photactive nature of azobenzene and self-assembly of pyridine to offer a unique library of photoactive materials.

Herein, we report control of excited-state photophysics with a single proton utilizing a set of three pyridine-based azo dyes (Figure 1). Systematic study of azo dyes quantifies (1) how the position of the pyridine heteroatom relative to the azo bond impacts the electronic and protonation properties of the dye, and (2) how the ability of the dyes to undergo two distinct, sequential protonation events impacts its photoisomerization capability. A combination of spectroscopic and computational techniques including UV-vis-monitored acid titrations, visible-light (453 nm) photoisomerizations, density functional theory (DFT) and time-dependent density functional theory (TDDFT) calculations are used to elucidate the mechanisms driving the

photoisomerization and the dramatic shut off of photoisomerization caused by protonation in these pyridine-based azo dyes.

Experimental.

Materials: 2-(p-dimethylaminophenyl)azopyridine (**Pyr2**) was purchased from Tokyo Chemical Industry (TCI). 3-(p-dimethylaminophenyl)azopyridine (**Pyr3**) and 4-(p-dimethylaminophenyl)azopyridine (**Pyr4**) were purchased from DSK Biopharma Inc. All dyes were used as acquired after their purities were verified via ^{1}H-NMR on a Bruker NMR operating at 400MHz (Figures S1 – S3). **Pyr4** was found to be unstable under ambient conditions and was stored in a freezer and used within 2 weeks of acquisition. Samples for both steady-state and transient absorption spectroscopy were prepared in acetonitrile that was dried over 4Å molecular sieves overnight. p-Toluenesulfonic acid (TosOH) was purchased from Millipore Sigma and used as received. Stock solutions of TosOH were prepared at 147 mM in dry acetonitrile and used to protonate **Pyr2**, **Pyr3** and **Pyr4**.

Instrumentation: Steady-state absorption spectra were collected using an Ocean Insight Flame UV-vis diode array spectrometer. A 1-ms integration time was used, and 100 scans were averaged for each collection. A boxcar width of 3 was used, which provides a spectral resolution of 1 nm. A Luzchem LED Illuminator equipped with an LEDi-RGB illuminator head was used to perform photoisomerization experiments. LEDs with illumination wavelengths of 453 nm (blue), 522 nm (green) and 634 nm (red) were used. The LEDi-RGB photoreactor head was calibrated by positioning a Coherent FieldMax II power meter at ~1 cm distance from the illuminator head, which is the same distance the LEDi is positioned from the samples during experiments. The output power of the lamp was measured as a function of increasing current loads through each color of LED. Currents used for calibration were 0.00 A, 0.01 A, 0.05 A, 0.10 A, 0.20 A, 0.50 A and 1.00 A and produced powers of 0 mW, 4 mW, 61 mW, 76 mW, 105 mW, 283 mW, and 411 mW respectively.

Photometric Acid Titrations: Photometric titrations (Figure 2) were performed by preparing solutions of dyes **Pyr2**, **Pyr3**, or **Pyr4** at 1.2 μM in acetonitrile. A portion of the 1.2 μM dye solution was then used to create a solution 1.2 μM in dye and 6.5 mM in TosOH solution. The titration experiment was performed by adding the acidified solution into the unprotonated solution and collecting UV-vis spectra of the solution between additions. Additional volumes began as 0.1 μL additions of the 6.5 mM TosOH / 1.2 μM dye solution to an initial sample of 2.0 mL of 1.2 μM dye and were gradually increased by increments of 0.1 – 1000 μL as additional acid was required to produce a change in the dyes' absorption spectra. In most titrations, 10 mL of acid solution was ultimately added to the 2.0 mL initial sample volume to reach complete protonation. The concentration of acid at each step of the titration was calculated using the volumes of the acidified solution added, calculating the number of moles of acid added, and dividing by the total solution volume.

Non-aqueous pK_a *determination:* The first and second pK_a values of **Pyr2**, **Pyr3**, and **Pyr4** were calculated from the acid titration data. Nonlinear fits were performed in MatLab using the Thordarson Fitting Program software package provided by Pall Thordarson in his Chemical Society Reviews article.[51] The association constants were determined by using a non-linear binding isotherm model describing the binding of a guest (G) to a host (H) molecule by simultaneously fitting at four absorption wavelengths using the expression,

$$\Delta A_{obs} = \frac{\varepsilon_{\Delta HG} K_1 [G] + \varepsilon_{\Delta HG} [H]_0 K_1 K_2 [G]^2}{1 + K_1 [G] + K_1 K_2 [G]^2} \quad (1)$$

where ΔA_{obs} is the change in absorbance taken from the beginning of the titration at a given wavelength, $\varepsilon_{\Delta HG}$ is the change in molar absorptivity between unbound and bound dyes, K_1 and K_2 are the binding constants for first and second protonation events respectively, $[H]_0$ is the total concentration of dye (which remains constant throughout the course of the titration) and [G] is the concentration of added TosOH. The fitting program determines the best fit of the data from a plot of ΔA_{obs} vs [G] to produce the binding constants of the first and second binding event. For each dye, wavelengths were selected that were at or near maxima of the first and second protonation states of each dye and are outlined specifically in Figure S6. Additional wavelengths were selected that exhibit minimal signal convolution between the various protonation states. Association constants determined from fitting were used to calculate the pK_a of each protonatable site ($pK_{a,azo}$) *via* the relationship,

$$pK_{a,azo} = -\log\left(\frac{1}{K}\right) + pK_{a,TosOH} \quad (2)$$

where K is the association constant for either of the two binding events (K_1 or K_2 from equation 1) and p$K_{a,TosOH}$ is the acidity constant of the p-toluenesulfonic acid, which is taken from the literature to be 8.5.[52] The trend in pK_a between dyes is also predicted computationally as described below (Table S1).

Photoisomerization: Photoisomerization studies were carried out using the Ocean Insight UV-vis spectrometer in combination with the Luzchem photolysis lamp. The lamp head of the photoreactor was positioned ~ 1 cm above the samples of dye in order to both minimize scattering into the fiber optic of the diode array and to maximize exposure of the sample to the incident light from the lamp head. Acid concentrations to reach the first and second protonation state of each dye were determined using the results of UV-vis photometric acid titrations. For **Pyr2** (1.2 μM), 2.4 eq of TosOH were added to reach the first protonation state and 583 eq were added to reach the second protonation state. For **Pyr3** (1.7 μM), 4.7 eq of TosOH were added to reach the first protonation state and 181 eq were added to reach the second protonation state. For **Pyr4** (1.6 μM), 0.9 eq of TosOH were added to reach the first protonation state and 67 eq were added to reach the second protonation state.

When illuminating the unprotonated dyes, the change in absorbance due to isomerization was found to be too rapid to capture with our steady-state spectrometer. Instead, a change in the absorption spectrum corresponding to the *trans* → *cis* isomerization was observed that changes with the illumination intensity. This observation implies that the relative rates of

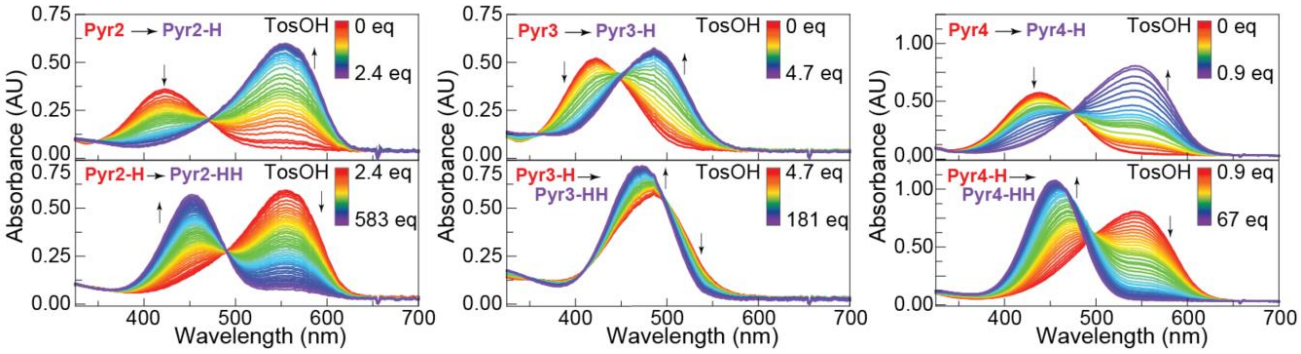

Figure 2. Titration of **Pyr2**, **Pyr3**, and **Pyr4** using TosOH in acetonitrile results in a shift in absorption spectrum.

isomerization and reversion of the dyes from *cis* to *trans* is fast enough in both directions to reach a steady state within our instrument response time. If reversion was fast and conversion was slow, we would see no change in absorbance at any illumination intensity, whereas if conversion was fast and reversion was slow then a full conversion could be observed at any illumination intensity. Due to this fast rate of conversion and reversion, the absorbance of each dye was collected as a function of illumination intensity rather than time to visualize the clean conversion of the *trans*- to *cis*-isomer. The absorption spectra of the dyes were collected at illumination intensities of 0 mW, 4 mW, 61 mW, 76 mW, 105 mW, 283 mW, and 411 mW using a blue-light LED.

Quantum Mechanical Calculations: Density Functional Theory (DFT) and time-dependent density functional theory (TDDFT) were carried out in Gaussian 16[53,54] at the CAM-B3LYP/6-311G(d,p)[55,56] level of theory. Diffuse functions were used in the basis set (6-311++G(d,p))[57] for dihedral angle scans in order to better describe the S_1 and S_2 excited states. A polarized continuum model was used to simulate an acetonitrile solvent environment. The CAM-B3LYP functional was chosen for its accurate experimental prediction of the relative positions of each dyes unprotonated, singly protonated and doubly protonated ground-state absorption spectra.

Potential energy curves for the ground (S_0) and excited states (S_1, S_2) were generated by performing an optimization scan while rotating the CNNC dihedral angle around the azo bond in steps of 5 degrees. Once ground-state geometries were acquired, TDDFT calculations were used to predict the potential energy surfaces of the S_1 and S_2 singlet excited states by assuming that the geometries (electron densities) of the ground state closely resemble the geometries of the excited state along the dihedral rotation.

To validate our experimental pK_a values, we used a DFT cluster continuum solvation model to approximate the first and second pK_a values of the pyridine-based azo dyes.[58,59] The pK_a values of **Pyr2**, **Pyr3** and **Pyr4** in acetonitrile (MeCN) (Eq. 2) were predicted using the solvation free energy from the exchange of a proton between a particular azo dye and a dimer of MeCN (Eq. 3). A temperature of 298.15 K was assumed and the density of MeCN at that temperature was used along with the molecular weight to predict the bulk solvent concentration ([MeCN]).[60]

$$\mathrm{p}K_\mathrm{a} = \frac{\Delta \mathrm{G_{sol}}}{\ln(10)\mathrm{RT}} - \log[\mathrm{MeCN}] \quad (3)$$

$$\Delta \mathrm{G_{sol}} = \mathrm{G^{eff}_{(2MeCN)-H}} + \mathrm{G^{eff}_{Azo}} - \mathrm{G^{eff}_{2(MeCN)}} - \mathrm{G^{eff}_{Azo-H}} \quad (4)$$

Here, the energy (G) was approximated by the sum of the electronic and thermal energies. To avoid using unnecessary empirical parameters, we calculated the energy of the various molecules (or solvent clusters) with the universal continuum solvation model (SMD).[61] The SMD model improves upon the popular PCM model by using the full solute electron density rather than partial atomic charges and results in generally smaller errors when calculating solvation free energies. For the pK_a values **Pyr2** and **Pyr3**, we additionally considered the energetic contributions from both rotational isomers (E/Z) by computing a Boltzmann weighted average of their energies.

$$\mathrm{G^{eff}} = \sum_\mathrm{i} \mathrm{W_i G_i} \quad (5)$$

$$\mathrm{W_i} = \frac{\mathrm{e^{-\epsilon_i/k_B T}}}{\sum_\mathrm{i} \mathrm{e^{-\epsilon_i/k_B T}}} \quad (6)$$

Results & Discussion.

1. *Protonation state characterization*

Additions of p-Toluenesulfonic acid (TosOH) to **Pyr2**, **Pyr3** and **Pyr4** (Figure 2) resulted in two sequential shifts in absorption indicating two distinct protonation events. The various protonation states of each pyridine-based azo dye are indicated using the abbreviated dye name followed by **-H** (or **-HH**). For instance, **Pyr2-H** is the singly protonated and **Pyr2-HH** is the doubly protonated version of **Pyr2**. Optimized energies of the protonated forms of all the dyes show that the first protonation for each dye occurs on the N heteroatom of the pyridine (N_{pyr}) (Table S3). The second protonation for all dyes occurs at the azo N closest to the heteroatom-containing ring (N_{azo}).

Pyr2 and **Pyr3** possess two distinct structural isomers of each of the *trans* and *cis*, based on the rotation of the N_{pyr} heteroatom relative to the azo bond, that can be optimized. These structures are not observed in **Pyr4**, because the N_{pyr} is symmetric with respect to the N=N azo bond. These structures are designated *E* and *Z* (Figure 3) to differentiate them from the *cis* and *trans* isomers. The *E* isomer of **Pyr2** and **Pyr3** is the most stable in the unprotonated state (by 52 meV in **Pyr2**, 26 meV in **Pyr3**). In the singly protonated dyes, the *Z* isomer is 42 meV more stable in **Pyr2-H** while the *E* isomer is 13 meV more stable in **Pyr3-H**. In the stable **Pyr2-H** *Z* isomer, the N_{pyr} proton is close

enough to the azo bond nitrogen (N3) to undergo intramolecular hydrogen bonding. Finally in both the doubly protonated dyes **(-HH**), the *Z* isomers are most stable (by 14 meV in **Pyr2-HH**, 13 meV in **Pyr3-HH**).

Absorption maxima of the unprotonated species and each protonation state for **Pyr2**, **Pyr3** and **Pyr4** are listed in Table 1 and shown in Figure 4 with computed transitions. The first experimental spectral shift (from **PyrN** to **PyrN-H,** Figure 4) occurs within 5 equivalents of acid and is marked by a significant bathochromic shift in all dyes. For **Pyr2** → **Pyr2-H** and **Pyr4** → **Pyr4-H**, the peaks shift from that of the unprotonated dye by 132 nm and 106 nm respectively, whereas for **Pyr3** → **Pyr3-H** it shifts significantly less (by only 64 nm). This shift results from a stabilization of the lowest unoccupied molecular orbital (LUMO, Figure S10) of each dye. The second protonation event (from **PyrN-H** to **PyrN-HH**, Figure 4) results in a hypsochromic shift in all dyes due to significant stabilization of the highest occupied molecular orbital (HOMO). For **Pyr2-H** → **Pyr2-HH** and **Pyr4-H** → **Pyr4-HH**, the peaks shift by 102 nm and 89 nm respectively, whereas the absorbance peak shifts by only 19 nm for **Pyr3-H** → **Pyr3-HH**. All three unprotonated dyes have absorption maxima within 10 nm of one another (Figure S4). However, notably, the absorption maximum of **Pyr3-H** is redshifted by 50 nm less than **Pyr2-H** and **Pyr4-H**. The difference in the magnitude of the redshifting arises from a reduced stabilization of the LUMO in **Pyr3-H** compared to **Pyr2-H** and **Pyr4-H**. The absorption maxima of all three doubly protonated spectra are within 15 nm of one another once again. Figure S8 shows the predicted TDDFT transitions for *trans* (*E* and *Z*) and *cis* (*E* and *Z*) for each protonation state. Addition of excess pyridine (a scavenger base) to a sample of **Pyr2-HH** recovered the spectrum of the unprotonated dye **Pyr2**, indicating reversibility of both protonation events.

Experimentally-determined pK_a values of the first protonation (Table S1) of **Pyr2**, **Pyr3** and **Pyr4** are 14.9±0.5, 13.0±0.7 and 13.5±0.1, respectively. Computational pK_a values agree with the trend observed in the experimental values. The relative first pK_a values correlate with the *ortho*/*para* vs *meta*-location of the N_{pyr} heteroatom. We posit that the similarities between the singly protonated **Pyr2-H** and **Pyr4-H** absorption spectra as compared to **Pyr3-H** are caused by the similar electronic interaction between the *ortho* and *para* positions of the pyridine nitrogen with respect to the azo bond.

In contrast, the second-protonation pK_a values increase from 11.3±0.2 in **Pyr2** to 11.4±0.1 in **Pyr3** and then to 13.8±0.3 in **Pyr4**. The pK_a values increase with the distance of the N_{pyr} heteroatom (first protonation site) from the N_{azo} (second protonation site). Thus, the relative position of the positive charge that develops at the N_{pyr} site during the first protonation drives the relative acidity of the second-protonation site.

2. Characterization of photoisomerization behavior

Photoisomerization of **Pyr2**, **Pyr3**, and **Pyr4** shows similar spectroscopic behavior in all of the dyes. Before the addition of any acid, all three dyes undergo a change in absorbance typical of *trans* → *cis* isomerization (Figure S7). In these dyes, this change is experimentally marked by a decrease in the

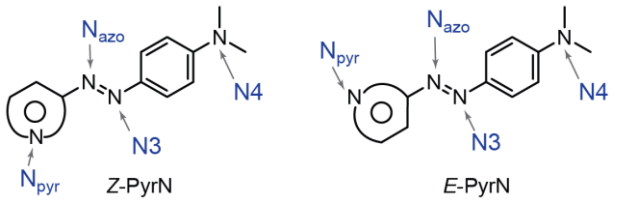

Figure 3. *E* and *Z* rotational isomers of **Pyr2** and **Pyr3**. The *E* vs *Z* label are derived from the relative position of the N_{pyr} with respect to the azo bond. The *E* and *Z* isomers are not observed in **Pyr4** because the N_{pyr} is symmetric with respect to the N=N azo bond.

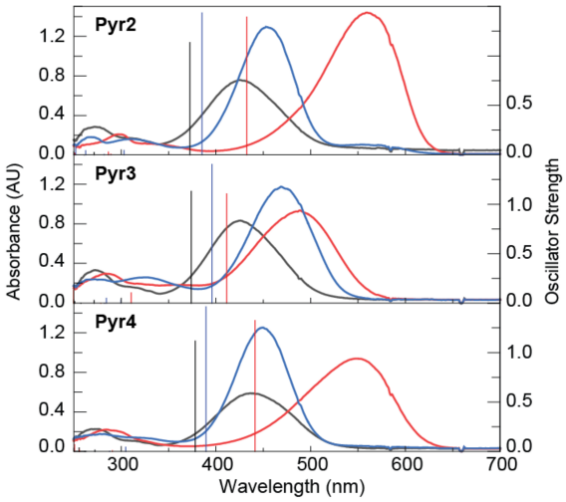

Figure 4. UV-vis spectra of unprotonated (black), singly protonated (red) and doubly protonated (blue) **Pyr2**, **Pyr3** and **Pyr4** with TDDFT-calculated transitions overlaid. CAM-B3LYP/6-311G(d,p)/PCM(MeCN). Transitions for the lowest energy for of each isomer are shown. All *E* and *Z* structures and transitions (Figure S9) are available in the SI.

absorbance of the S_2 absorption peak (*e.g.* 425 nm in **Pyr2**) and an increase in a peak blueshifted from that peak by about 50 nm (*e.g.* 375 nm in **Pyr2)**. This shift is consistent with the known increase in molar absorptivity of the n → π* S_1 absorption of the *cis* isomer, resulting from increased orbital overlap when the associated orbitals are in closer physical proximity.[16] TDDFT calculations (Figure S9) show a peak at longer wavelengths than the *trans* isomer's absorption maximum corresponding to the S_0 → S_1 excitation of the *cis*-isomer of each dye.[17] In addition, TDDFT predicts that the *cis*-isomer's π → π* (S_0 → S_2) transition is blueshifted and less probable (smaller oscillator strength from decreased orbital overlap) than the *trans*-isomer, as seen in the experimental spectra. **Pyr3** undergoes the slightly more conversion to the *cis*-isomer with 0.56±0.7 of the *trans*-isomer remaining upon illumination compared to 0.62±0.10 and 0.59±0.06 of the **Pyr2** and **Pyr4** *trans*-isomers remaining upon photolysis, respectively (Table S2 and Figure S7).

Photoisomerization of the dyes in ***both*** the first (**-H**) ***and*** second (**-HH**) protonation state was not observed (Figure S7). Protonated dyes were illuminated at the maximum power of 411 mW for the blue LED (453 nm). **Pyr2-H** and **Pyr4-H** were also illuminated at maximum power of 143.7 mW for the green LED (522 nm), due to their redshifted absorption spectra and no

Table 1. Absorption maxima and experimentally determined pK_a values of **Pyr2**, **Pyr3** and **Pyr4**.[§]

	λ_{max}[‡] **PyrN**	λ_{max}[‡] **PyrN-H**	λ_{max}[‡] **PyrN-HH**	$pK_{a,1}$[†]	$pK_{a,2}$[†]
Pyr2	425	561	452	14.9 (0.8)	11.3 (0.2)
Pyr3	425	491	467	14.6 (0.4)	11.4 (0.1)
Pyr4	435	543	449	15.3 (1.2)	13.8 (0.3)

[‡] All wavelengths reported in nm. [†] Standard deviations reported in parentheses.

[§]The pK_a values derived from DFT are shown in the Supporting Information in Table S1 and match the trend observed experimentally.

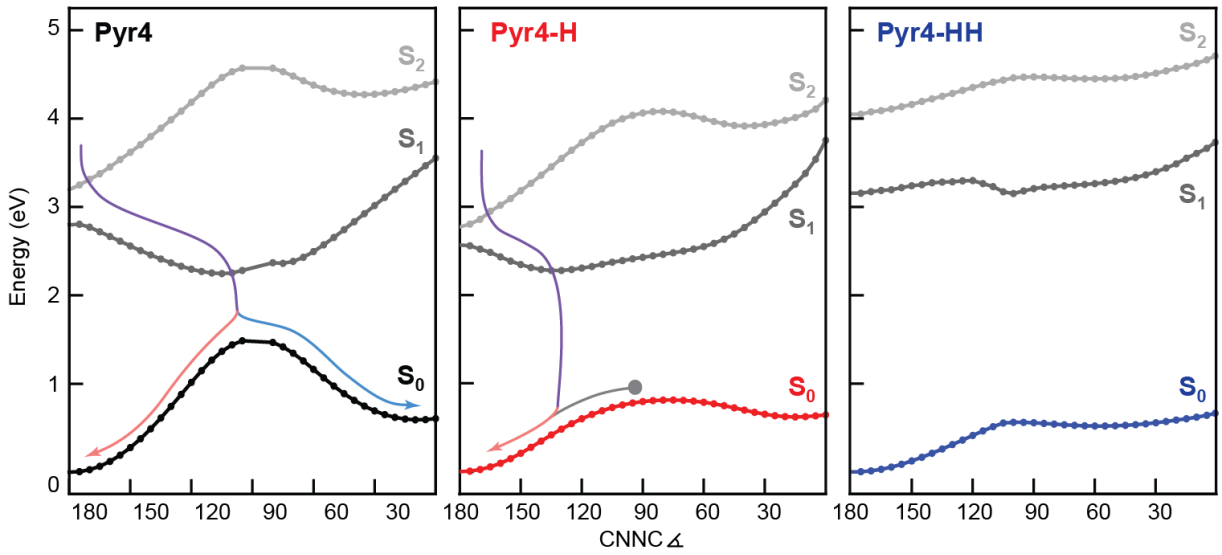

Figure 5. Potential energy curves along the S_0 surface of unprotonated (black, left tile), singly (red, middle tile) and doubly (blue, right tile) protonated **Pyr4** along C-N=N-C dihedral angle. Arrows show the proposed mechanism for the deactivation pathway in unprotonated, singly and doubly protonated molecules. CAM-B3LYP/6-311++G(d,p)/PCM(acetonitrile) optimized scans along the S_0 surfaces with single point TDDFT S_1 and S_2 computed at the same geometries are points plotted above. PECs for **Pyr2** and **Pyr3** in all protonated forms are shown in Figure S16.

change was observed. A longer attempt at photoisomerization was carried out on **Pyr2-HH** and no spectral shift was observed over the course of 16 hours (Figure S11). These results are surprising given that the ***first protonation takes place on the pyridine nitrogen*** and therefore does not structurally block either rotation or inversion of the azo bond.

The impact on the photoisomerization must therefore be an electronic one, which can be rationalized using potential energy curves (PECs) of the ground state (S_0), and the S_1 and S_2 excited states. As expected, the photoisomerization of the unprotonated occurs through a rotation (∠CNNC azo) mechanism after relaxing from $S_2 \rightarrow S_1$ (Figure 5, Figure S16-27). This mechanism is supported by our PECs that show rotation as an energetically downhill process in the S_1 excited state (Figure S17). Even though initially downhill, neither of the two possible inversion mechanisms (either on the pyridine or phenyl side) form a conical intersection with the S_0 or have an energetic minimum near the *cis*-isomer in either the S_1 or S_2 excited states. Additionally, the pseudo-optimized lowest excited-state (S_1) structures of **Pyr2** and **Pyr4** (Figure S15) were predicted to have a similar geometry to the S_1 minima from the dihedral rotation reaction coordinate.

In the PECs, S_2 and S_1 meet in a conical intersection near the *trans*-isomer allowing internal conversion from the spin-allowed excitation to S_2 into the spin-forbidden S_1 state. The S_1 state then relaxes via CNNC rotation along the excited state surface, crossing back to the ground state at a conical intersection (∠CNNC ~ 90°) (Figure 5, **Pyr4** purple line) that permits rotational relaxation to either the ground state (S_0) *cis*- or *trans*-isomer (Figure 5, **Pyr4** blue or red line, respectively). In the singly-protonated molecule (**-H**), however, the S_1 state is predicted to relax to an excited-state minimum (∠CNNC ~ 135°) that deactivates into a "hot" *trans*-isomer on the S_0 surface (Figure 5, **Pyr4-H** purple line), making formation of the *cis*-isomer unfavorable. Neither inversion mechanism would suggest the formation of the *cis-isomer* following the same arguments for each of the dyes (**PyrN-H**, Figure S17). In the doubly protonated dyes (**-HH**), the S_2 and S_1 states do not meet in a conical intersection at the *trans* geometry like they do in the unprotonated and singly protonated state, meaning once again that no deactivation pathway is likely to yield the ground state *cis*-isomer. However, the phenyl inversion path in the doubly protonated **PyrN-HH** can preferentially invert in the S_2 state to meet at a conical intersection with the S_1 at ~142° (Figure S17).

From this point it is energetically uphill to invert any further, making isomerization unlikely. Furthermore, in the singly and doubly protonated dyes, the barrier to revert from *cis* to *trans* on the S_0 surfaces is significantly lower than in the unprotonated dyes, so any population of *cis*-isomer is expected to quickly revert to the *trans*-isomer.

Conclusions

In summary, photophysical measurements and computations were carried out on a series of three pyridine-based azo dyes; **Pyr2**, **Pyr3**, and **Pyr4**. Acid titrations using TosOH revealed that the three dyes can undergo two sequential protonation events marked by the observation of distinct isosbestic points in the absorptions spectra. DFT calculations concluded that the first protonation on each dye occurs at the pyridine N position, and the second protonation occurs at the closest azo N position to the pyridine moiety. Nonlinear simultaneous analysis of absorption versus acid concentration at multiple wavelengths revealed that **Pyr2** and **Pyr4** had higher first pK_a values (14.9 and 15.3 respectively) than **Pyr3** (14.6), however for the second protonation, the pK_a values increased going from the 2- to 3- to 4-position on the pyridine N. The trend in first-protonation pK_a value is associated with the *ortho/para* directing nature of the azo bond on the pyridine heteroatom. The trend in second protonation is associated with the distance-dependent inductive effect of the first proton on the second protonation site.

Illumination of unprotonated **Pyr2**, **Pyr3** and **Pyr4** resulted in rapid bulk photoisomerization from the *trans*- to *cis*-isomer, with a reversion rate on a similar order as the isomerization rate. Photoisomerization was shut down in all the dyes upon the addition of acid even though first protonation takes place on the pyridine nitrogen and does not directly interact with the azo bond. Interrogation of the ground- and excited-state potential energy curves between the *trans*- and *cis*-isomer revealed that the isomerization is blocked by a shift of the S_1 minimum away from the rotational barrier, as well as a reduction in the ground-state (reversion) isomerization barriers in both protonated states, resulting either in no formation of the *cis*-isomer or rapid reversion to the *trans*-isomer that resulted in no observed population of *cis*-isomer. The difference in these mechanisms should be discernable via time resolved spectroscopy and we are currently making efforts in this direction.

Author Contributions

ERY and LAF conceptualized the project and reviewed and edited the manuscript. SMM and ZJK contributed equally to the writing of the original draft. SMM collected experimental data, ZJK and IAT collected computational data. IAT, KE, KS and AJ validated portions of the experimental and computational data.

Conflicts of interest

There are no conflicts to declare.

Acknowledgements

ERY and LAF thank The Pittsburgh Foundation for funding (UN2020-114823). This work made use of the Lehigh University (LU) NMR Facility (NSF-MRI-1725883, with support from LU). Portions of this research were conducted with research computing resources provided by LU and the TG-CHE190011 allocation from XSEDE, which is supported by NSF grant number ACI-1548562. Financial support also comes from LU.

Notes and references

1 A. Bafana, S. S. Devi and T. Chakrabarti, *Environ. Rev.*, 2011, 19, 350–370.
2 M. P. Placidi, A. J. L. Villaraza, L. S. Natrajan, D. Sykes, A. M. Kenwright and S. Faulkner, *J. Am. Chem. Soc.*, 2009, **131**, 9916–9917.
3 C. Cobbold, *Ambix*, 2019, **66**, 23–50.
4 R. O. Alves de Lima, A. P. Bazo, D. M. F. Salvadori, C. M. Rech, D. de Palma Oliveira and G. de Aragão Umbuzeiro, *Mutat Res Genet Toxicol Environ Mutagen*, 2007, **626**, 53–60.
5 E. Akceylan, M. Bahadir and M. Yilmaz, *J Hazard Mater*, 2009, **162**, 960–966.
6 A. Anastasi, F. Spina, V. Prigione, V. Tigini, P. Giansanti and G. C. Varese, *Bioresour Technol*, 2010, **101**, 3067–3075.
7 Z. Ai, J. Li, L. Zhang and S. Lee, *Ultrason Sonochem*, 2010, **17**, 370–375.
8 M. Aleksić, H. Kušić, N. Koprivanac, D. Leszczynska and A. L. Božić, *Desalination*, 2010, **257**, 22–29.
9 A. A. Ahmad and B. H. Hameed, *J Hazard Mater*, 2010, **175**, 298–303.
10 A. Bafana, S. S. Devi, K. Krishnamurthi and T. Chakrabarti, *Appl. Microbiol. Biotechnol.*, 2007, **74**, 1145–1152.
11 D. Saini, R. Aggarwal, A. K. Sonker and S. K. Sonkar, *ACS Appl Nano Mater*, 2021, **4**, 9303–9312.
12 G. Mezohegyi, A. Kolodkin, U. I. Castro, C. Bengoa, F. Stuber, J. Font, A. Fabregat and A. Fortuny, in *Ind. Eng. Chem.*, 2007, vol. 46, pp. 6788–6792.
13 S. Crespi, N. A. Simeth, A. Bellisario, M. Fagnoni and B. König, *J. Phys. Chem. A*, 2019, **123**, 1814–1823.
14 S. W. Magennis, F. S. Mackay, A. C. Jones, K. M. Tait and P. J. Sadler, *Chem. Mater.*, 2005, **17**, 2059–2062.
15 N. A. Simeth, S. Crespi, M. Fagnoni and B. König, *J. Am. Chem. Soc.*, 2018, **140**, 2940–2946.

16 H. M. D. Bandara and S. C. Burdette, *Chem Soc Rev*, 2012, **41**, 1809–1825.

17 S. Crespi, N. A. Simeth and B. König, *Nat Rev Chem*, 2019, 3, 133–146.

18 R. Mogaki, K. Okuro and T. Aida, *J Am Chem Soc*, 2017, **139**, 10072–10078.

19 J. Calbo, C. E. Weston, A. J. P. White, H. S. Rzepa, J. Contreras-García and M. J. Fuchter, *J Am Chem Soc*, 2017, **139**, 1261–1274.

20 J. Ewert, L. Heintze, M. Jordà-Redondo, J.-S. von Glasenapp, S. Nonell, G. Bucher, C. Peifer and R. Herges, *J Am Chem Soc*, 2022, **144**, 15059–15071.

21 Y. Chong, X. Zhang, B. Chen, R. Liu, Z. Wu, G. Zhang, J. Jiang, S. Mukamel and G. Zhang, *J Phys Chem A*, 2021, **125**, 3088–3094.

22 S. Ludwanowski, M. Ari, K. Parison, S. Kalthoum, P. Straub, N. Pompe, S. Weber, M. Walter and A. Walther, *Chem Euro J*, 2020, **26**, 13203–13212.

23 I. K. Lednev, T. Ye, R. E. Hester and J. N. Moore, *J Phys Chem*, 1996, **3654**, 13338–13341.

24 I. K. Lednev, T. Q. Ye, P. Matousek, M. Towrie, P. Foggi, F. V. R. Neuwahl, S. Umapathy, R. E. Hester and J. N. Moore, *Chem Phys Lett*, 1998, **290**, 68–74.

25 J. Azuma, N. Tamai, A. Shishido and T. Ikeda, *Chem Phys Lett*, 1998, **288**, 77–82.

26 C. Slavov, C. Yang, L. Schweighauser, C. Boumrifak, A. Dreuw, H. A. Wegner and J. Wachtveitl, *Phys Chem Chem Phys*, 2016, **18**, 14795–14804.

27 C. J. Otolski, A. M. Raj, V. Ramamurthy and C. G. Elles, *Chem Sci*, 2020, **11**, 9513–9523.

28 M. Quick, A. L. Dobryakov, M. Gerecke, C. Richter, F. Berndt, I. N. Ioffe, A. A. Granovsky, R. Mahrwald, N. P. Ernsting and S. A. Kovalenko, *J Phys Chem B*, 2014, **118**, 8756–8771.

29 F. Aleotti, L. Soprani, A. Nenov, R. Berardi, A. Arcioni, C. Zannoni and M. Garavelli, *J Chem Theory Comput*, 2019, **15**, 6813–6823.

30 Y. Hirose, H. Yui and T. Sawada, *J Phys Chem A*, 2002, **106**, 3067–3071.

31 G. Hartley, *Nature*, 1937, **140**, 281.

32 A. N. Oldacre and E. R. Young, *RSC Adv*, 2020, **10**, 14804–14811.

33 A. N. Oldacre, C. A. Pointer, S. M. Martin, A. Kemmerer and E. R. Young, *Chem. Commun*, 2019, **5874**, 5874.

34 J. Rickhoff, N. B. Arndt, M. Böckmann, N. L. Doltsinis, B. J. Ravoo and L. Kortekaas, *J Org Chem*, 2022, **87**, 10605–10612.

35 M. S. Scholz, J. N. Bull, N. J. A. Coughlan, E. Carrascosa, B. D. Adamson and E. J. Bieske, *J Phys Chem A*, 2017, **121**, 6413–6419.

36 H. Ren, P. Yang and F. M. Winnik, *Polym Chem*, 2020, **11**, 5955–5961.

37 H. Ren, X. P. Qiu, Y. Shi, P. Yang and F. M. Winnik, *Macromolecules*, 2019, **52**, 2939–2948.

38 X. Su and I. Aprahamian, *Org Lett*, 2011, **13**, 30–33.

39 X. Su and I. Aprahamian, *Org Lett*, 2013, **15**, 5952–5955.

40 K. Nakashima, A. Georgiev, D. Yordanov, Y. Matsushima, S. I. Hirashima, T. Miura and L. Antonov, *J Org Chem*, 2022, **87**, 6794–6806.

41 Nakashima K., Petek A., Hori Y., Georgiev A., Hirashima S., Matsushima Y., Yordanov D., Miura T. and Antonov L., *Chem Euro J*, 2021, **27**, 11559–11566.

42 R. Smolka, D. Yordanov, K. Nakashima, M. Vala, J. Krajčovič, M. Weiter and A. Georgiev, *Dyes and Pigments*, 2023, **215**, 111279.

43 Y. Ni, X. Li, J. Hu, S. Huang and H. Yu, *Chem Mater*, 2019, **31**, 3388–3394.

44 A. I. Kovalchuk, Y. L. Kobzar, I. M. Tkachenko, Y. I. Kurioz, O. G. Tereshchenko, O. V. Shekera, V. G. Nazarenko and V. V. Shevchenko, *ACS Appl Polym Mater*, 2020, **2**, 455–463.

45 L. Cui and Y. Zhao, *Chem Mater*, 2004, **16**, 2076–2082.

46 C. Egami, Y. Kawata, Y. Aoshima, S. Alasfar, O. Sugihara, H. Fujimura and N. Okamoto, *Jpn. J. Appl. Phys*, 2000, **39**, 1558–1561.

47 C. L. Van Oosten, C. W. M. Bastiaansen and D. J. Broer, *Nat Mater*, 2009, **8**, 677–682.

48 M. Yamada, M. Kondo, J. I. Mamiya, Y. Yu, M. Kinoshita, C. J. Barrett and T. Ikeda, *Angew Chem Int Ed*, 2008, **47**, 4986–4988.

49 S. Serak, N. Tabiryan, R. Vergara, T. J. White, R. A. Vaia and T. J. Bunning, *Soft Matter*, 2010, **6**, 779–783.

50 T. Michinobu, R. Eto, H. Kumazawa, N. Fujii and K. Shigehara, *J Macromol Sci A*, 2011, **48**, 625–631.

51 P. Thordarson, *Chem Soc Rev*, 2011, **40**, 1305–1323.

52 A. Kütt, S. Tshepelevitsh, J. Saame, M. Lõkov, I. Kaljurand, S. Selberg and I. Leito, *European J Org Chem*, 2021, **2021**, 1407–1419.

53 M. J. Frisch, G. W. Trucks, H. B. Schlegel, G. E. Scuseria, M. A. Robb, J. R. Cheeseman, G. Scalmani, V. Barone, G. A. Petersson, H.

Nakatsuji, X. Li, M. Caricato, A. V. Marenich, J. Bloino, B. G. Janesko, R. Gomperts, B. Mennucci, H. P. Hratchian, J. V. Ortiz, A. F. Izmaylov, J. L. Sonnenberg, D. Williams-Young, F. Ding, F. Lipparini, F. Egidi, J. Goings, B. Peng, A. Petrone, T. Henderson, D. Ranasinghe, V. G. Zakrzewski, J. Gao, N. Rega, G. Zheng, W. Liang, M. Hada, M. Ehara, K. Toyota, R. Fukuda, J. Hasegawa, M. Ishida, T. Nakajima, Y. Honda, O. Kitao, H. Nakai, T. Vreven, K. Throssell, Jr. J. A. Montgomery, J. E. Peralta, F. Ogliaro, M. J. Bearpark, J. J. Heyd, E. N. Brothers, K. N. Kudin, V. N. Staroverov, T. A. Keith, R. Kobayashi, J. Normand, K. Raghavachari, A. P. Rendell, J. C. Burant, S. S. Iyengar, J. Tomasi, M. Cossi, J. M. Millam, M. Klene, C. Adamo, R. Cammi, J. W. Ochterski, R. L. Martin, K. Morokuma, O. Farkas, J. B. Foresman and D. J. Fox, 2016, Gaussian 16, Gaussian, Inc., Wallingford CT.

54 R. Dennington, T. Keith and J. Millam, 2016, GaussView, Semichem Inc., Shawnee Mission, KS.

55 T. Yanai, D. P. Tew and N. C. Handy, *Chem Phys Lett*, 2004, **393**, 51–57.

56 M. M. Francl, W. J. Pietro, W. J. Hehre, J. S. Binkley, M. S. Gordon, D. J. DeFrees and J. A. Pople, *J Chem Phys*, 1982, **77**, 3654–3665.

57 E. Papajak, J. Zheng, X. Xu, H. R. Leverentz and D. G. Truhlar, *J. Chem. Theory Comput*, 2011, **7**, 3027–3034.

58 J. R. Pliego, *Chem Phys Lett*, 2002, **367**, 145–149.

59 A. Malloum and J. Conradie, *Data Brief*, 2021, **37**, 107144.

60 G. A. K. O. I. Davydova, V. N. Afansev, B. A. Zhukov, *Zh.Fiz.Khim.*, 1986, **60**, 982–984.

61 A. V. Marenich, C. J. Cramer and D. G. Truhlar, *J Phys Chem B*, 2009, **113**, 6378–6396.